Supporting Information

Tuning *d*-Band Centers by Coupling PdO nanoclusters to WO₃ Nanosheets to Promote the Oxygen Reduction Reaction

Jun-Hyeong Lee[a,‡], DaBin Yim[a,‡], Jung-Hyun Park[a,‡], Chi Ho Lee[b], Jong-Min Ju[a], Sang Uck Lee[b,], and Jong-Ho Kim[a,*]*

a Department of Chemical Engineering, Hanyang University, Ansan 15588, Republic of Korea.

b Department of Bionano Technology and Department of Applied Chemistry, Hanyang University, Ansan 15588, Republic of Korea.

* To whom correspondence should be addressed: kjh75@hanyang.ac.kr,

sulee@hanyang.ac.kr

‡ These authors contributed equally to this paper.

1. *Materials and reagents* **:** Tungsten sulfide (WS_2) powder (≥99.8%), 20 wt% Pt/C (HiSPEC ®3000) and potassium tetrachloropalladate(II) (K_2PdCl_4) powder (≥99.99%) were purchased from Alfa Aesar. Molybdenum sulfide (MoS_2) powders (<2 μm, 99%), Nafion solution (5 wt% in EtOH), and n-butyllithium (1.6 M solution in hexanes) were purchased from Sigma-Aldrich. Acetonitrile (CH_3CN), ethanol (C_2H_5OH) and methanol (CH_3OH) were purchased from DAEJUNG chemicals & metal Co., LTD (Korea).

2. *Instrument* **:** Surface structures and morphology were characterized by transmission electron microscopy (TEM, JEM-2100F, JEOS/CEOS) and atomic force microscopy (AFM, XE-100, Park systems, Korea). Raman spectra were measured by Raman Spectroscopy (UniRAM, 532 nm). UV/Vis absorption spectra were measured by using a UV/Vis spectrometer (Mega 2100). X-ray photoelectron spectroscopy (XPS, AXIS-His, KRATOS, UK) was used to confirm the oxidation states of W, Mo and Pd atoms. The concentrations of WS_2 nanosheets and PdO on $PdO@WO_3S_x$ nanosheets were measured by inductive coupled plasma-atomic emission spectroscopy (ICP-AES, SPECTRO, SPECTRO ARCOS). The concentrations of Cl^- and SO_4^{2-} ions were measured by ion chromatography (IC, 882 Compact IC Plus, Metrohm, Switzerland). The electrocatalytic activity was tested using a potentiostat/galvanostat (VersaSTAT3, Princeton Applied Research, USA).

3. *Experimental methods*

A. *Synthesis of 1T-TMD nanosheets (MoS_2 & WS_2)* **:** A 15 mL of n-butyllithium in hexane solution (1.6 M) was added to 1g of bulk TMD powders in a round bottom flask at 25 °C under a N_2 atmosphere. Then, the reaction temperature was raised to 70 °C, and the mixture was stirred for further 48 h. After 48 h, the reaction solution was centrifuged at 100 × g for 10 min, and the obtained sediment was washed with hexane twice to remove the unreacted n-butyllithium and bulk TMDs. For the exfoliation of 1T-TMD nanosheets, 80 mL of DI water

was then added to the obtained sediment, followed by sonication for 1 h using a bath sonicator. The solution was centrifuged at 100 × g for 10 min to obtain the supernatant. The obtained supernatant was then dialyzed for 5 days to remove lithium cations. Finally, the dialyzed solution was centrifuged at 300 × g for 30 min, and then the supernatant containing exfoliated 1T-TMD nanosheets was collected.

B. *Reaction of 1T-TMD (MoS₂ & WS₂) nanosheets with Pd(OAc)₂ in CH₃CN* : The aquous solution of 1T-WS$_2$ nanosheets was centrifuged at 45,000 x g to exchange water with CH$_3$CN. After removing water from 1T-WS$_2$ nanosheets, they were washed with CH$_3$CN twice through a centrifugation and redispersion process. Then, the 1T-WS$_2$ nanosheets were dispersed in 20 mL of CH$_3$CN (25 μg/mL), followed by addition of 3 mg of Pd(OAc)$_2$. The resulting mixture was allowed to react by stirring at 50 °C for 1 h. The reaction solution was cooled and centrifuged at 15,000 rpm for 7 min to isolate the product. The product was washed with CH$_3$CN three times.

C. *Synthesis of free PdO nanoclusters* : The aquous solution of K$_2$PdCl$_4$ was stirred at 50 °C for 1 h. The reaction solution was cooled and centrifuged at 15,000 rpm for 7 min to isolate the product. The product was washed with DI water three times.

4. *Computational details* : All *ab initio* calculations were performed with the Vienna *Ab initio* Simulation Package (VASP 5.4.4).[1-4] We used the projector augmented wave (PAW) method[3-6] with the generalized gradient approximation based on the Perdew-Burke-Ernzerhof (PBE)[7] functional. A plane-wave cutoff energy of 500 eV was used. Lattice constants and internal atomic positions were fully optimized until the residual forces were less than 0.04 eV/Å. The vacuum slab space of a unit cell in the z-direction was set to 15 Å to avoid interactions between layers. The calculated lattice parameters of monoclinic-WO$_3$ and tetragonal-PdO are

7.67 Å and 3.10 Å, respectively. With the calculated lattice parameter, we constructed $WO_3(001)$ surface, which has proven to be the most stable surface in theoretical surface energy evaluation.[8] In addition, based on d-spacing value (0.265 and 0.215 nm) in HR-TEM analysis, we constructed two different PdO(101) and PdO(110) surface structures. The k-points of WO_3 and PdO surface structures were sampled using (3 x 3 x 1) Monkhorst-Pack mesh.[9] The schematics of our models are shown as Figure S12.

5. *Designing hybrid PdO@WO$_3$S$_x$ surface structures* : To explore the enhanced ORR catalytic activity in hybrid $PdO@WO_3S_x$ system, we preferentially investigated $PdO@WO_3S_x$ heterojunction structures using PdO(101), PdO(110) and $WO_3(001)$ surfaces, because PdO has d-spacing value of 0.265 and 0.215 nm, consistent with PdO(101) and PdO(110) in the HR-TEM image, and $WO_3(001)$ has been proven to be the most stable surface in theoretical surface energy evaluation.[8] Considering different types of surface termination and lattice mismatching between two surface structures (Figure S12), we constructed the four different hybrid models applied minimal strain to two surface structures, named by $PdO(101)_{PdO}@WO_3(001)_{WO}$, $PdO(110)_{Pd}@WO_3(001)_{WO}$, $PdO(110)_O@WO_3(001)_{WO}$, and $PdO(110)_{Pd}@WO_3(001)_O$. (Subscripts represent surface termination types) And then, we systematically screened various interface configurations that respective hybrid structure could have, because the interface in hybrid system significantly affects electronic property for ORR catalytic activity. From the calculated relative energies of all possible hybrid $PdO@WO_3S_x$ interface configurations by shifting along x-y in-plane directions between PdO(101), PdO(110) and $WO_3(001)$ structures as shown in Figure S13, we determined the most stable interface of each hybrid structure. Then, finally we confirmed $PdO(101)_{PdO}@WO_3(001)_{WO}$ and $PdO(110)_{Pd}@WO_3(001)_O$ as the energetically most favorable hybrid $PdO@WO_3S_x$ interfaces by using fully relaxed structure optimization. Given the well-established pure and

hybrid structures, we analyzed the electronic structures of them using the partial density of

state (PDOS) for understanding hybrid system effect on the enhanced ORR catalytic activity.
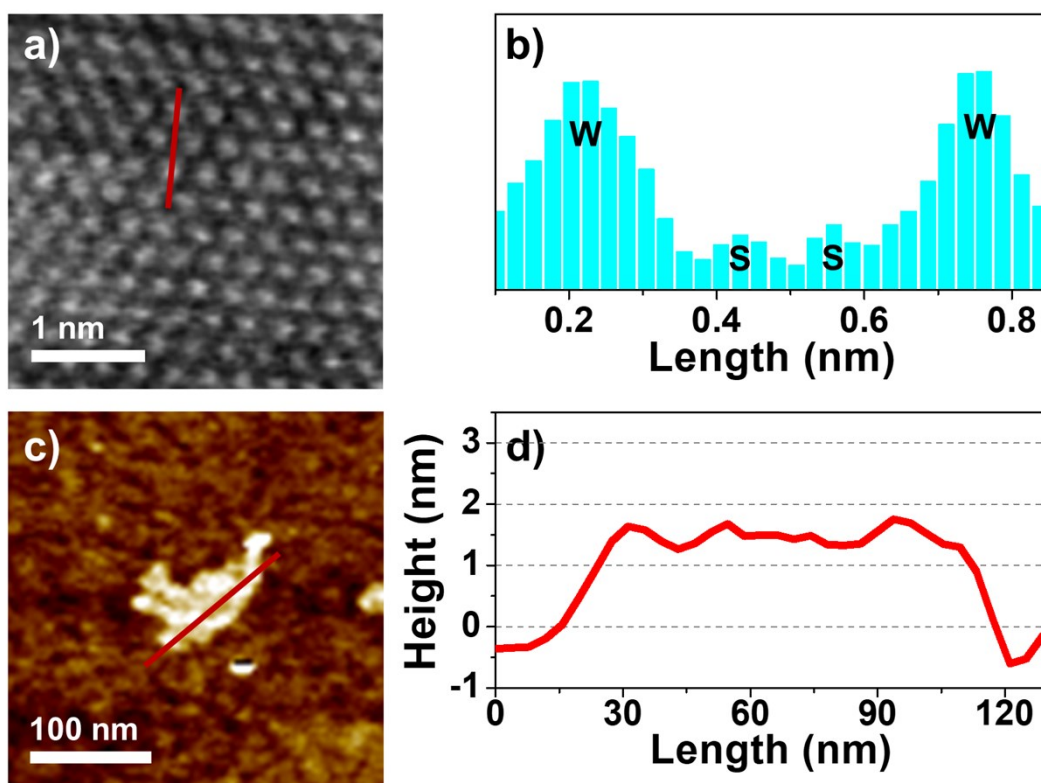
6. Supplementary Figures

Figure S1. (a) HR-TEM image, (b) atomic intensity profile, (c) AFM image, and (d) height profile of metallic 1T-WS$_2$ nanosheet.
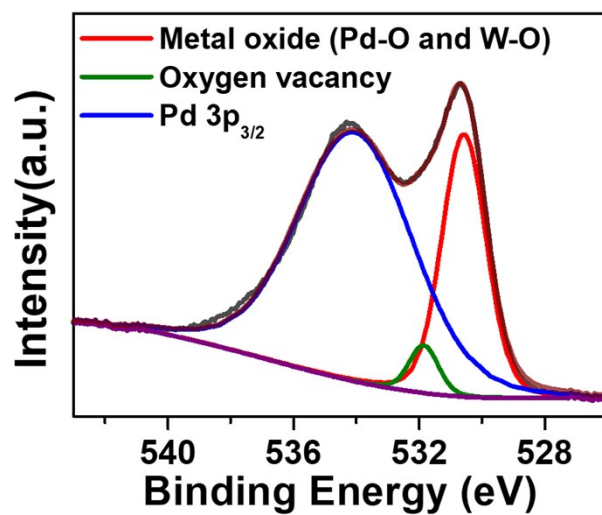
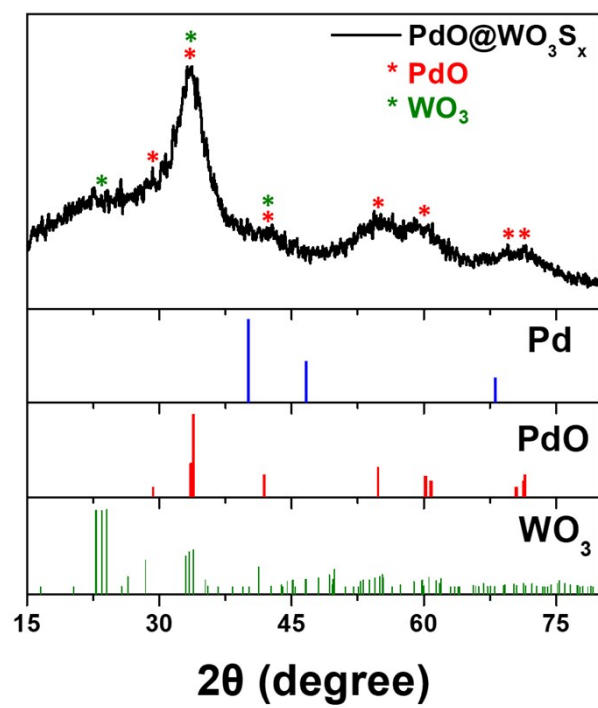***Figure S2***. O1s XPS spectrum of PdO@WO$_3$S$_x$.
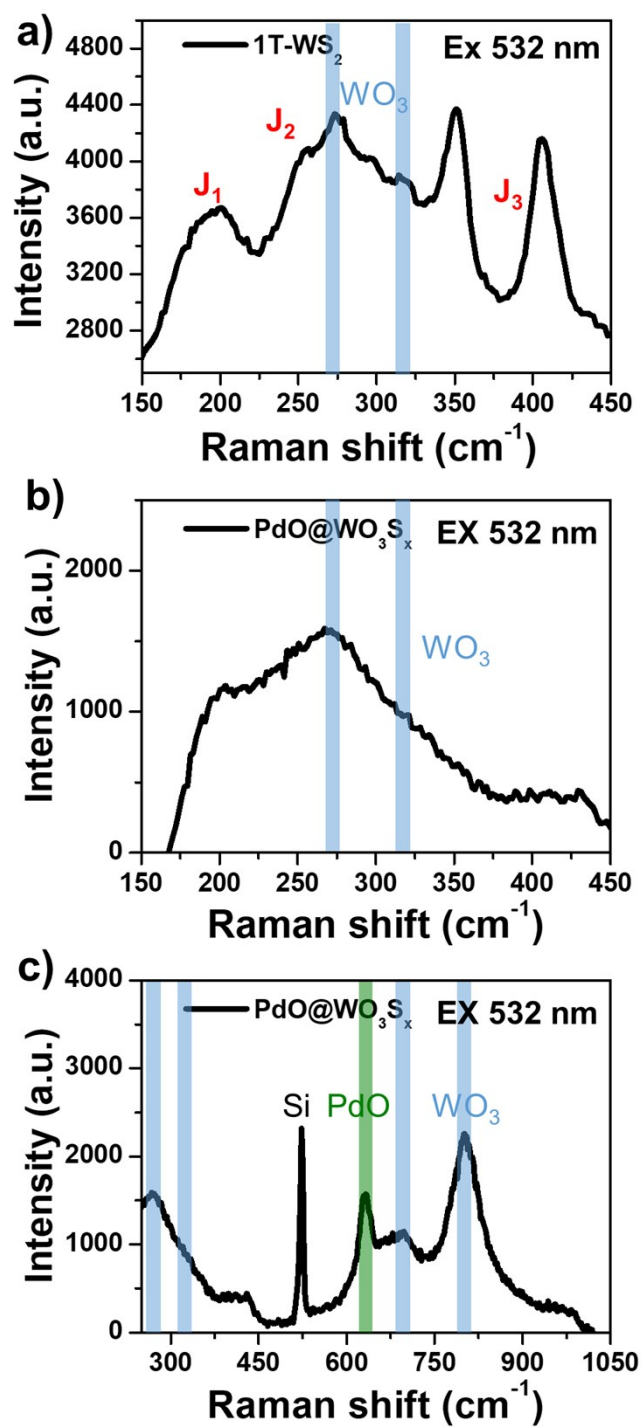
Figure S3. XRD patterns of PdO@WO$_3$S$_x$.

Figure S4. Raman spectra of (a) 1T-WS_2 nanosheets and (b)-(c) PdO@WO_3S_x hybrid.
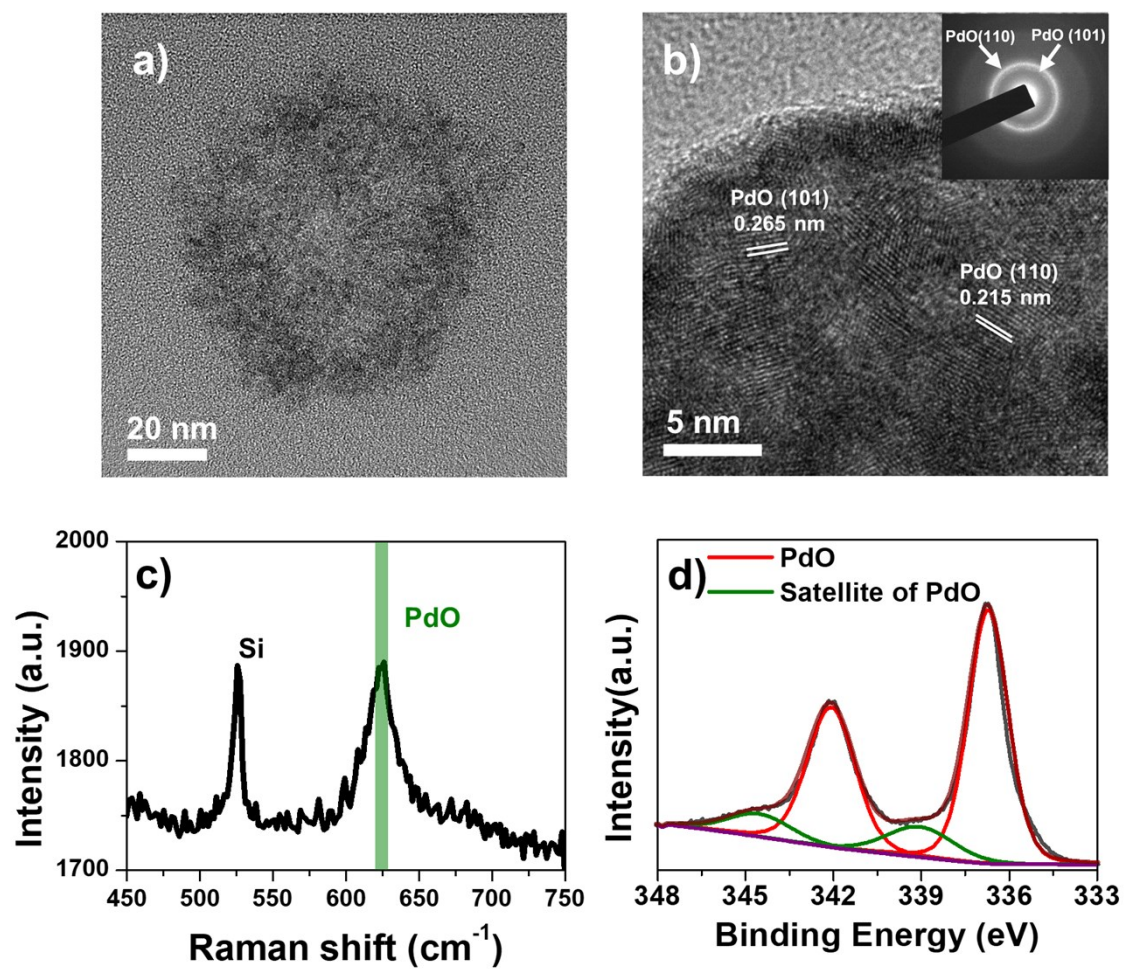
Figure S5. (a) TEM image, (b) HR-TEM image (inset: SAED pattern), (c) Raman spectrum, and (d) Pd3d XPS spectrum of pure PdO nanoclusters.
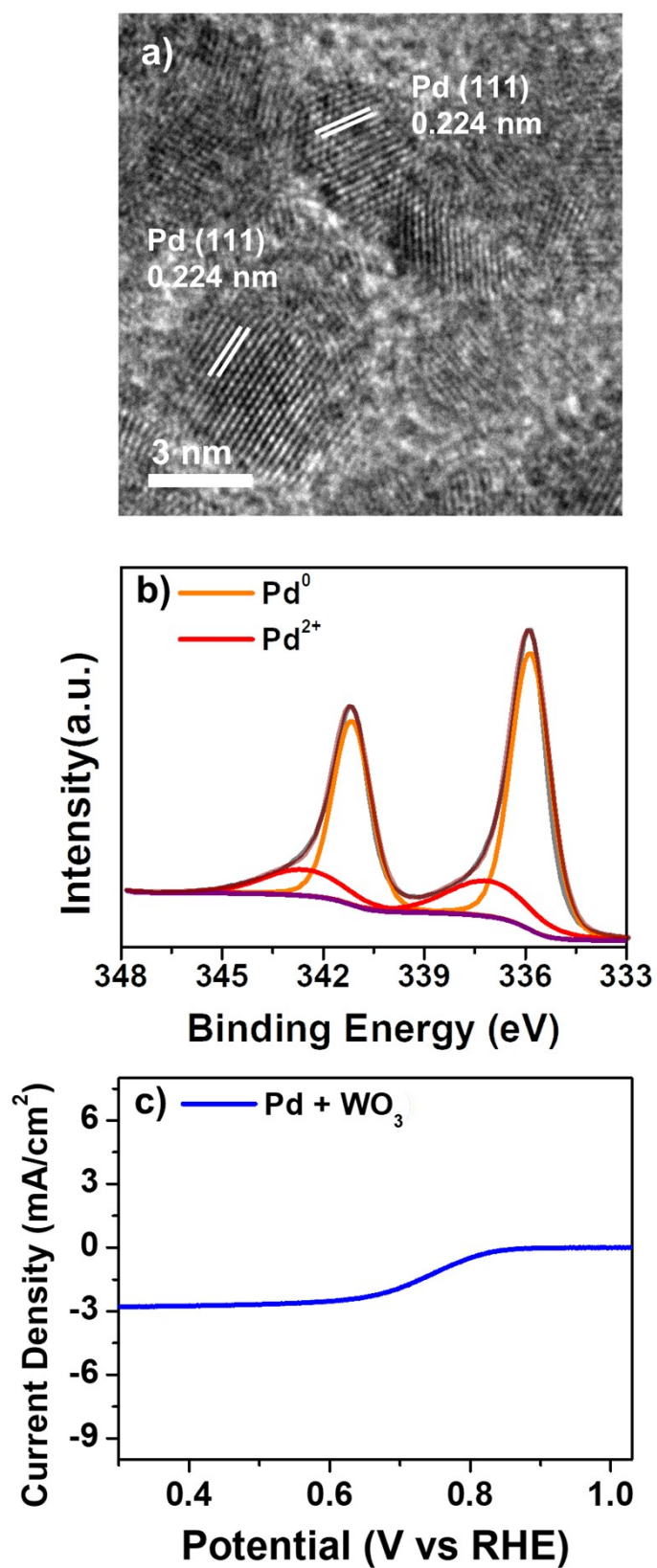
Figure S6. (a) TEM images, and (b) Pd3d XPS spectrum of Pd nanoparticles. (c) LSV curve of the physical mixture of Pd nanoparticles and WO_3 in the ORR.
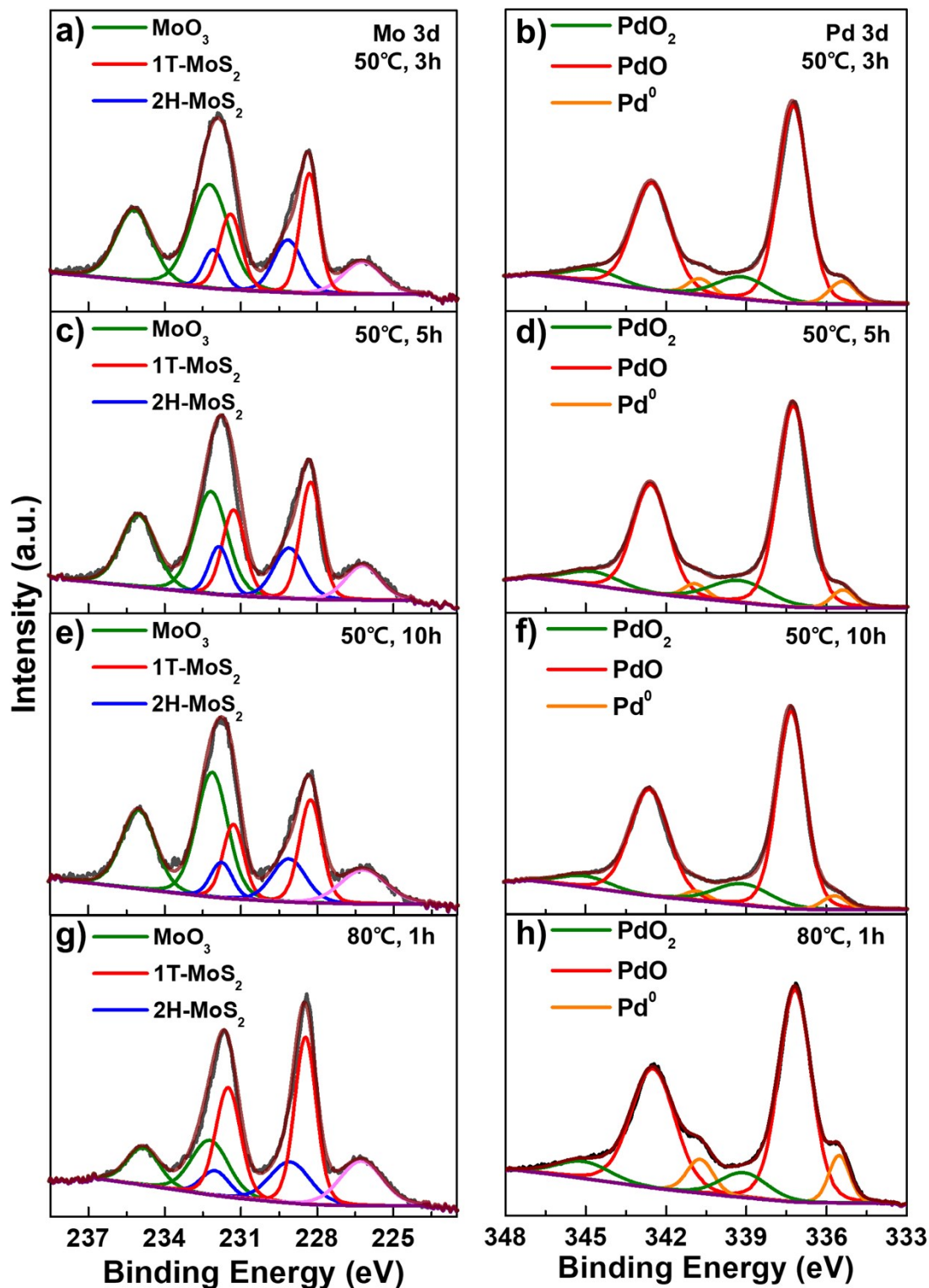
Figure S7. XPS spectra of the products for the reaction of 1T-MoS$_2$ with K$_2$PdCl$_4$ at various conditions. Mo3d and Pd3d XPS spectra of PdO@MoS$_x$O$_3$ hybrids synthesized at 50 ℃ for (a, b) 3h, (c, d) 5h, (e, f) 10h, and (g, h) at 80 ℃ for 1h.
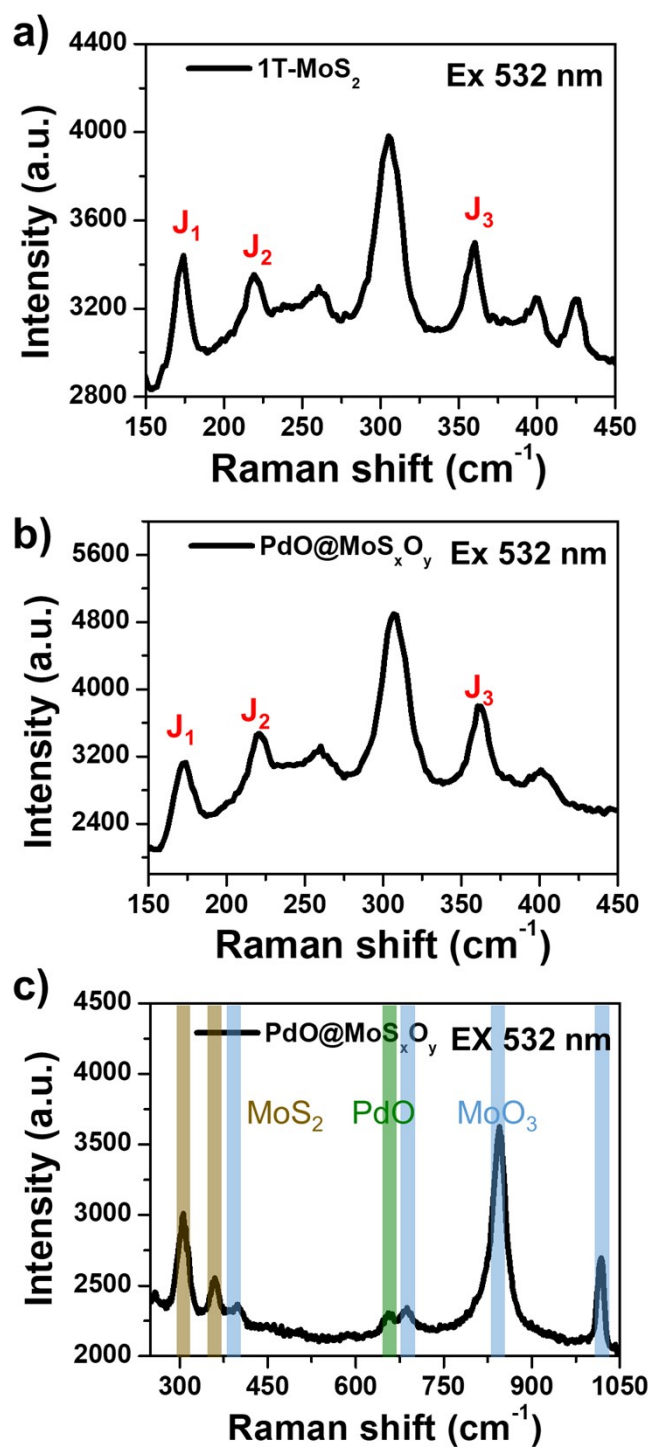
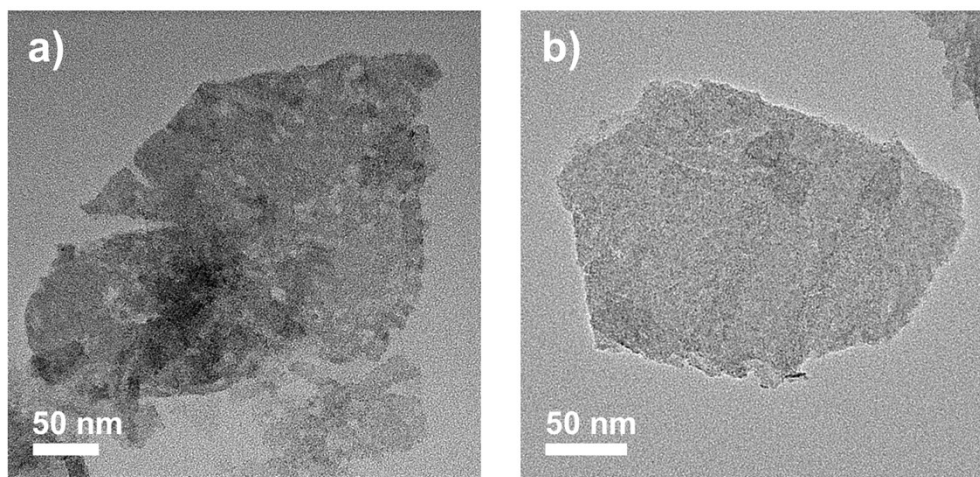***Figure S8.*** Raman spectra of (a) 1T-MoS_2 nanosheets and (b, c) PdO@MoS_xO_3 hybrid.

Figure S9. TEM images of the products after the reactions of Pd(OAc)$_2$ with (a) 1T-WS$_2$ and (b) 1T-MoS$_2$ in CH$_3$CN.
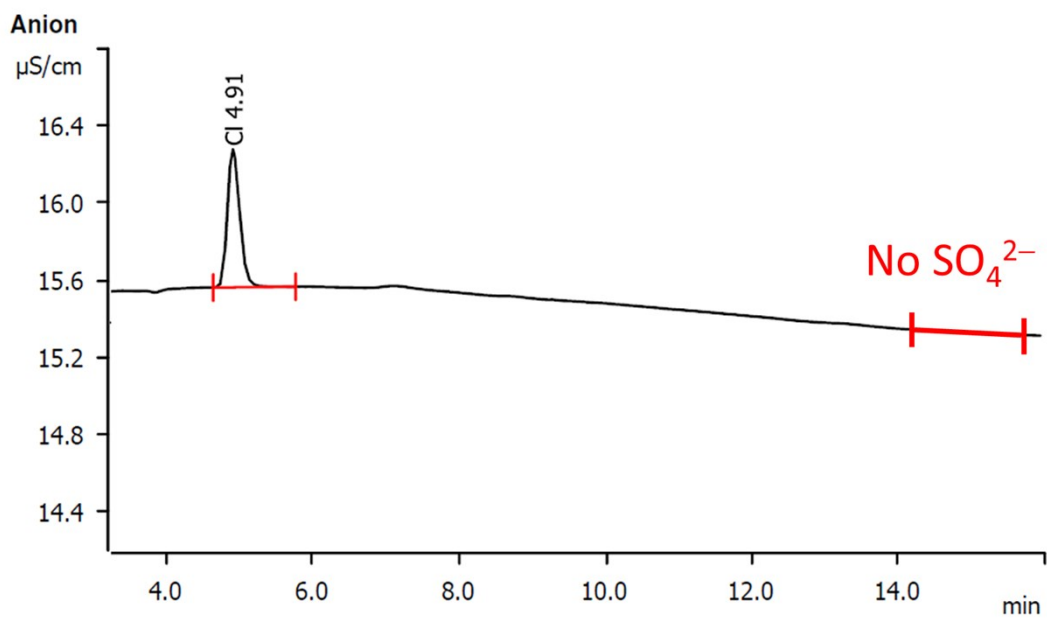
Figure S10. Ion chromatogram of the supernatant after completing the reaction of metallic 1T-WS$_2$ nanosheets with K$_2$PdCl$_4$ at 50 °C for 1 h in H$_2$O.
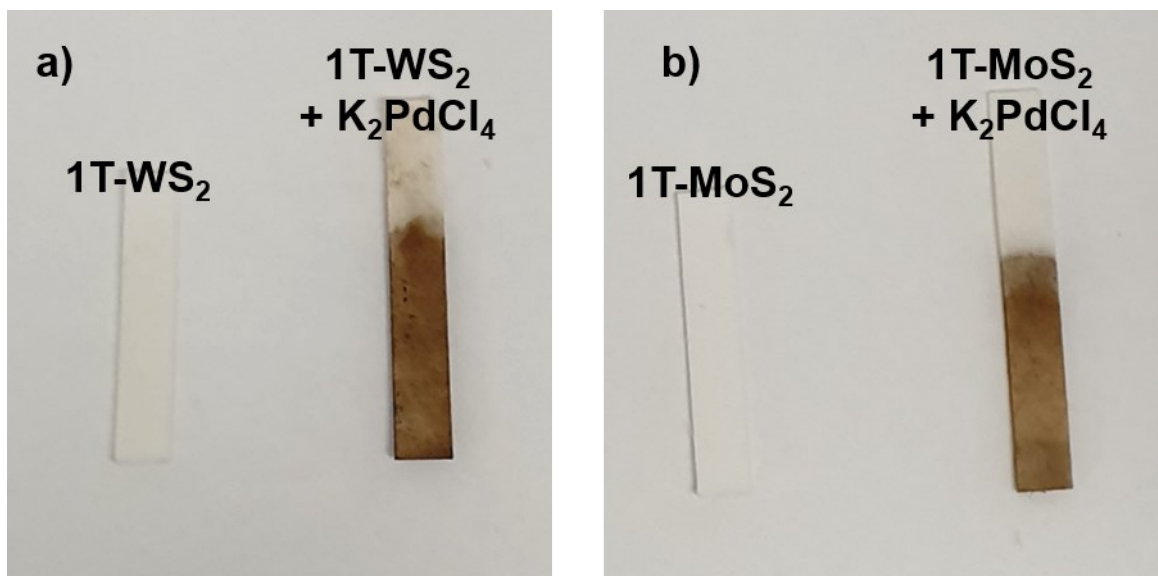
Figure S11. Colorimetric detection of H_2S in the supernatants of (a) 1T-WS$_2$ and PdO@WO$_3$S$_x$ and (b) 1T-MoS$_2$ and PdO@MoS$_x$O$_3$ reaction mixtures using a lead acetate paper strip.
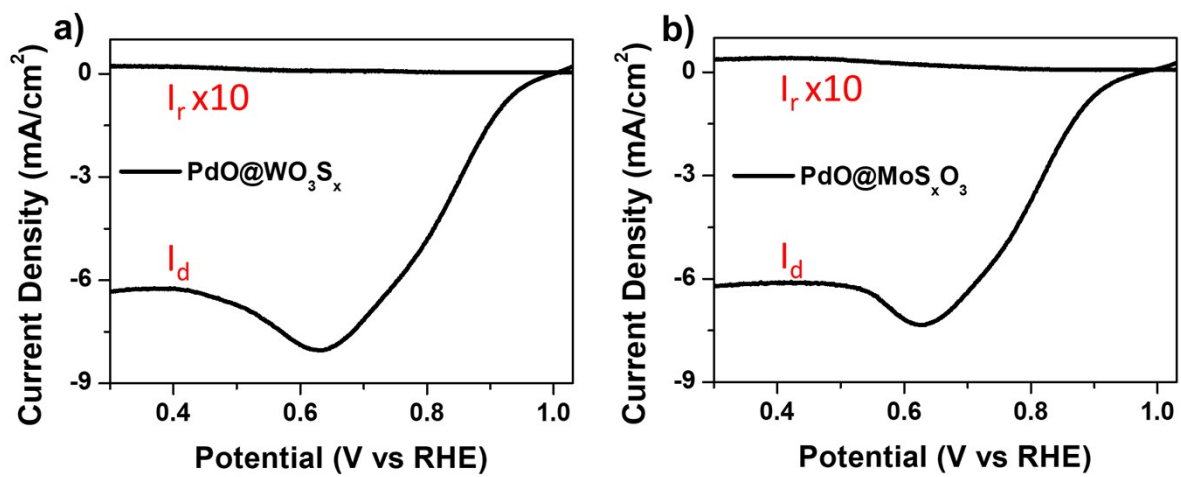
Figure S12. RRDE polarization curves for (a) $PdO@WO_3S_x$ and (b) $PdO@MoS_xO_3$ in an O$_2$-saturated 0.1 M KOH solution at 1,600 rpm.
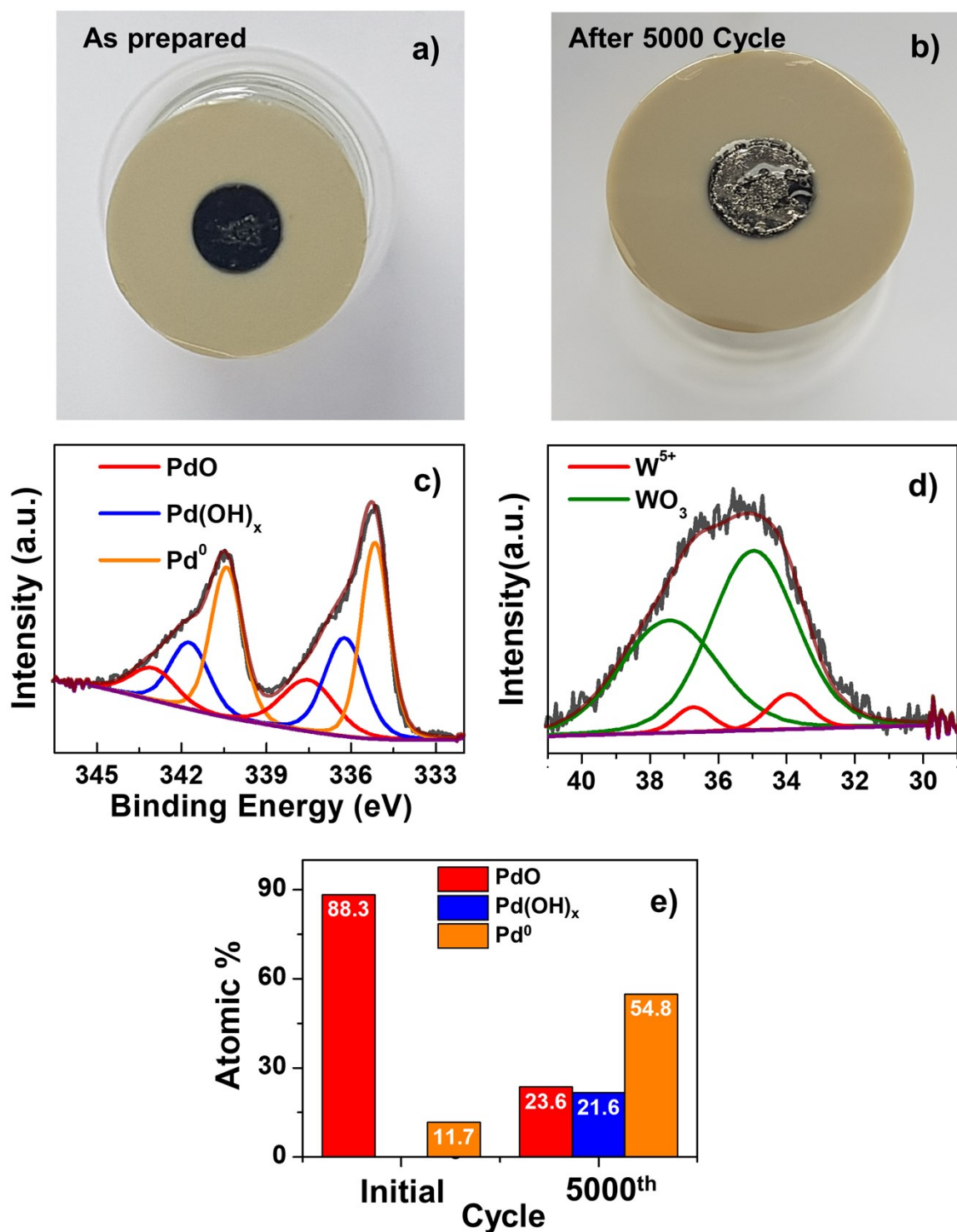
Figure S13. Optical images for PdO@WO$_3$S$_x$ electrodes (a) before and (b) after 5,000 cycles of ORR. XPS spectra for (c) Pd3d, and (d) W4f of the PdO@WO$_3$S$_x$ hybrid after 5,000 cycles of ORR in O$_2$-saturated 0.1 M KOH at 100 mV/s and 1,600 rpm. (e) Relative amounf of PdO, Pd^0, and Pd(OH)$_x$ in the PdO@WO$_3$S$_x$ electrode before and after 5,000 cycles of ORR.
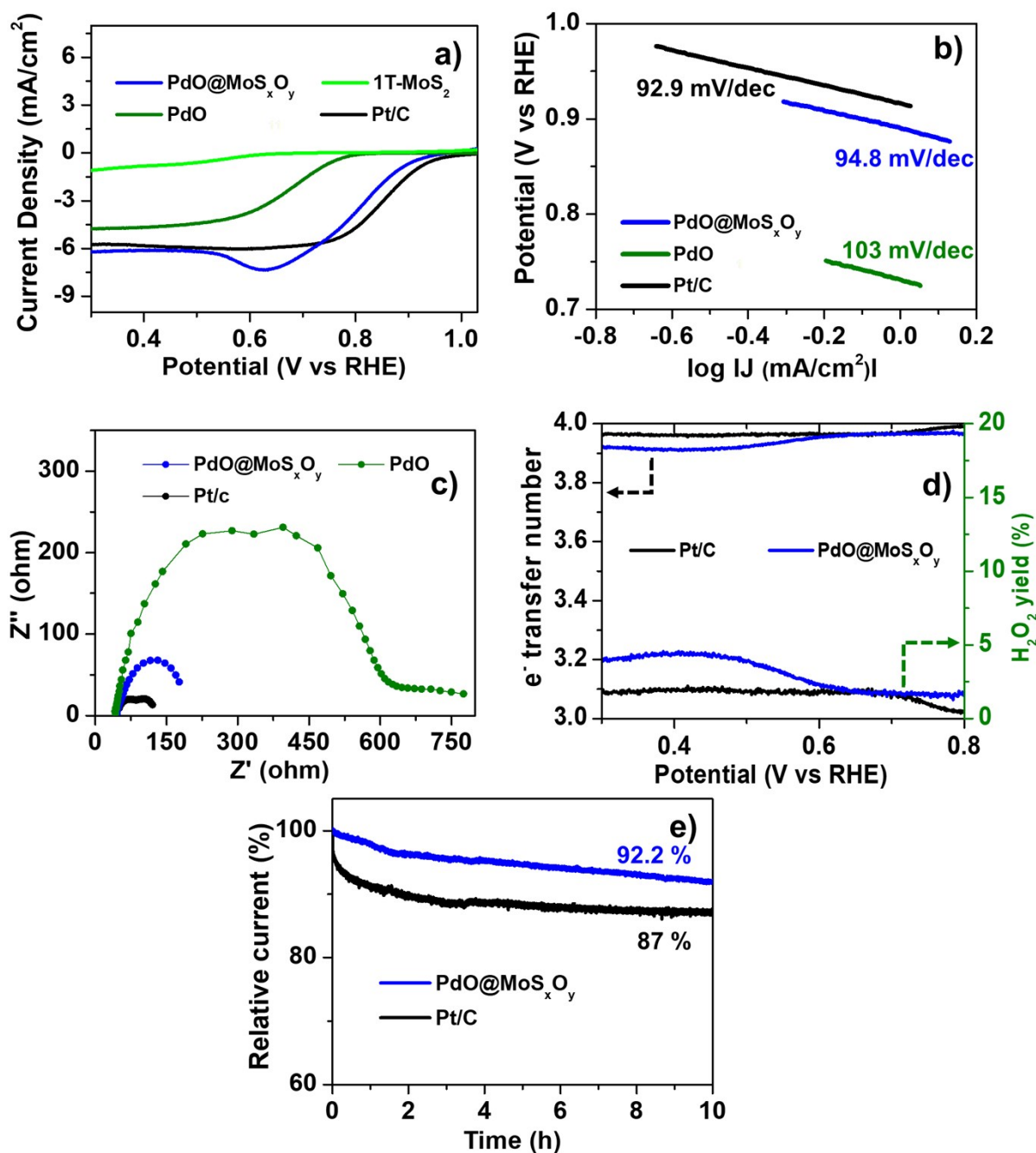
Figure S14. Electrocatalytic activity and durability of PdO@MoS$_x$O$_3$ hybrid for ORR. (a) LSV curves of PdO@MoS$_x$O$_3$ hybrid, pure PdO, 1T-MoS$_2$, and Pt/C for ORR. (b) Tafel plots for PdO@MoS$_x$O$_3$ hybrid, pure PdO nanoclusters, and Pt/C for ORR. (c) Nyquist plots of PdO@MoS$_x$O$_3$ hybrid, pure PdO nanoclusters, and Pt/C measured at 0.78 V (*vs*. RHE). (d) RRDE voltammogram-based electron transfer numbers and H$_2$O$_2$ production yields of PdO@MoS$_x$O$_3$ hybrid and Pt/C for ORR. (e) Chronoamperometric responses of PdO@MoS$_x$O$_3$ hybrid and Pt/C at 0.4 V (*vs*. RHE) for the continuous ORR process.
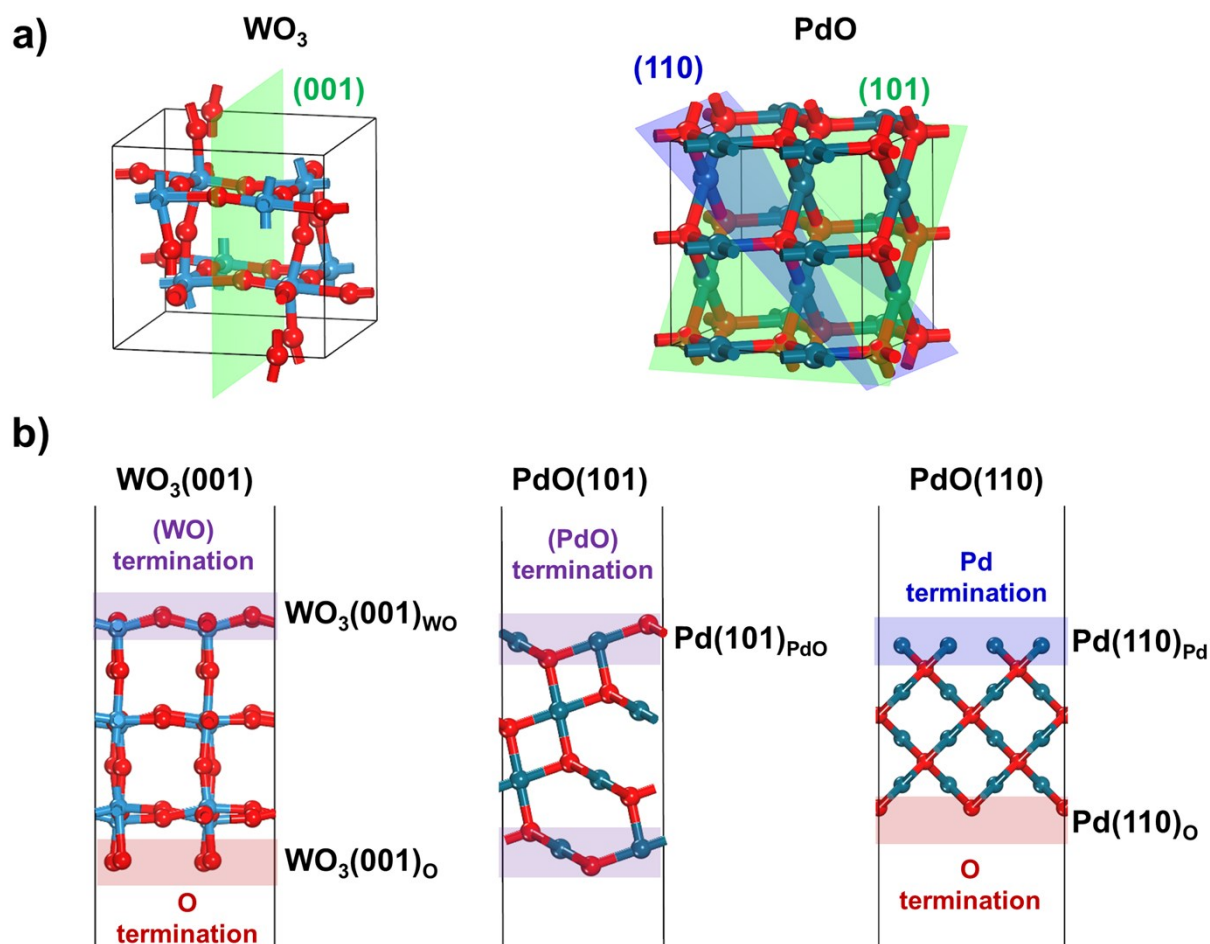
Figure S15. (a) Bulk and (b) surface structures of WO_3 and PdO, respectively.
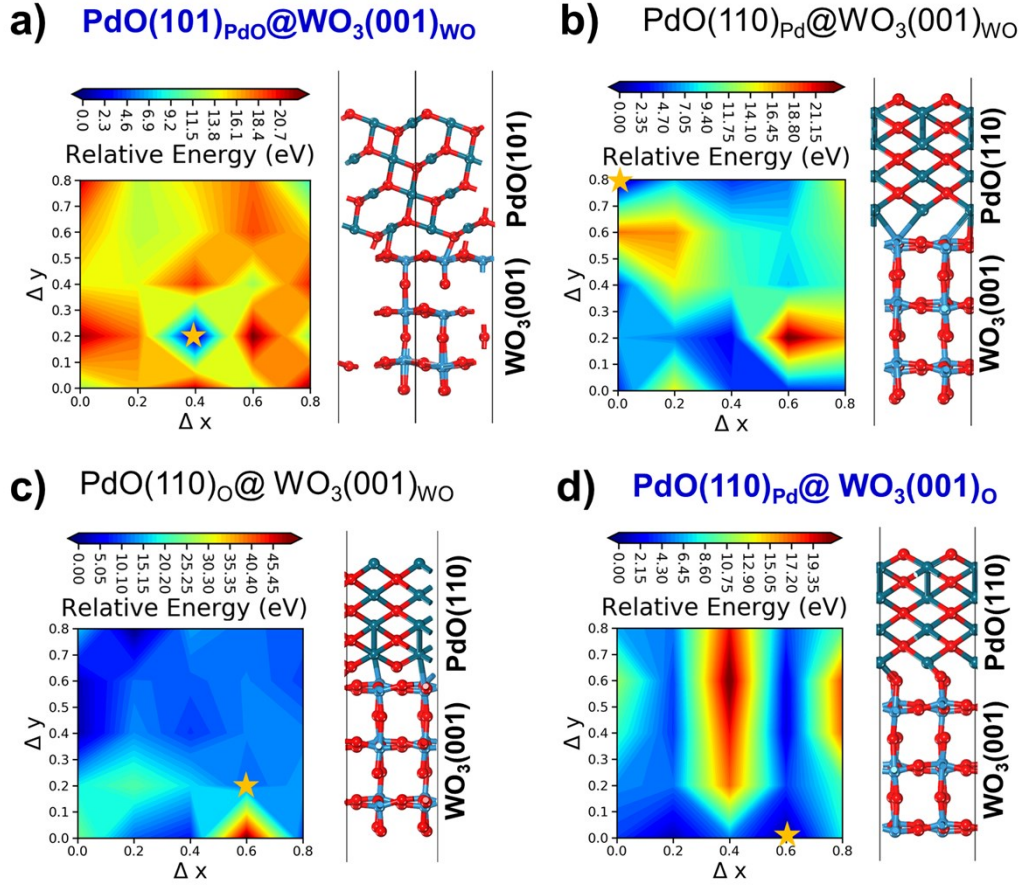
Figure S16. Scanning relative energies of all possible interface configurations of the hybrid PdO@WO$_3$S$_x$ by shifting along x-y in-plane directions between PdO(101), PdO(110) and WO$_3$(001) structures. (a) PdO(101)$_{PdO}$@WO$_3$(001)$_{WO}$, (b) PdO(110)$_{Pd}$@WO$_3$(001)$_{WO}$, (c) PdO(110)$_O$@WO$_3$(001)$_{WO}$ and d) PdO(110)$_{Pd}$@WO$_3$(001)$_O$. Orange stars represent the most stable hybrid structures.
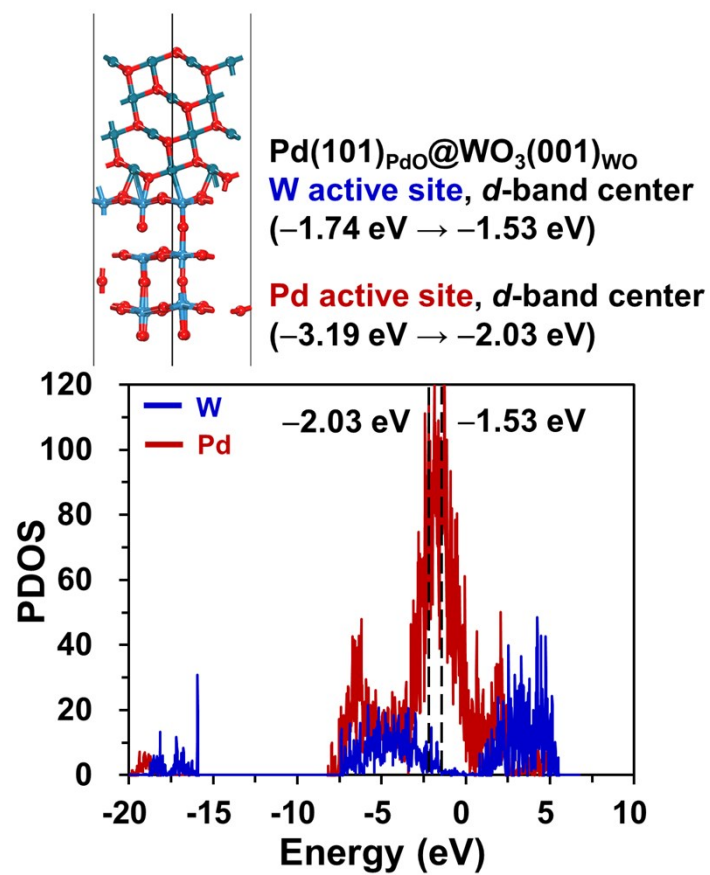
Figure S17. Partial density of states (PDOS) of PdO(101)$_{PdO}$@WO$_3$(001)$_{WO}$. Black dashed lines in PDOS indicate *d*-band centers.

Supplementary References

1 Kresse, G.; Hafner, J., Ab initio molecular dynamics for open-shell transition metals. *Phys. Rev. B* **1993,** *48*, 13115-13118.

2 Kresse, G.; Hafner, J., Ab initio molecular-dynamics simulation of the liquid-metal–amorphous-semiconductor transition in germanium. *Phys. Rev. B* **1994,** *49*, 14251-14269.

3 Kresse, G.; Furthmüllerb, J., Efficiency of ab-initio total energy calculations for metals and semiconductors using a plane-wave basis set. *Comp. Mater. Sci.* **1996,** *6*, 15-50.

4 Kresse, G.; Furthmüllerb, J., Efficient iterative schemes for ab initio total-energy calculations using a plane-wave basis set. *Phys. Rev. B* **1996,** *54*, 11169-11186.

5 Blöchl, P. E., Projector augmented-wave method. *Phys. Rev. B* **1994,** *50*, 17953-17979.

6 Kresse, G.; Joubert, D., From ultrasoft pseudopotentials to the projector augmented-wave method. *Phys. Rev. B* **1999,** *59*, 1758.

7 Perdew, J. P.; Burke, K., Generalized Gradient Approximation Made Simple. *Phys. Rev. Lett.* **1996,** *77*, 3865.

8 Rogal, J.; Reuter, K.; Scheffler, M., Thermodynamic stability of PdO surfaces. *Phys. Rev. B* **2004,** *69* (7), 075421.

9 Monkhorst, H. J.; Pack, J. D., Special points for Brillouin-zone integrations. *Phys. Rev. B* **1976,** *13*, 5188.